Springer

KSME

Journal of Mechanical Science and Technology 33 (8) (2019) 3871~3883
www.springerlink.com/content/1738-494x(Print)/1976-3824(Online)
DOI 10.1007/s12206-019-0731-1

Aerodynamic design and optimization of a high-loaded axial fan stage using a curvature control method †

Jieling Li[1], Huanlong Chen[1,2,*], Yang Liu[1], Junli Wang[1] and Xianqing Yang[2,3]

[1]*School of Energy Science and Engineering, Harbin Institute of Technology, Harbin 150001, China*
[2]*Yobow Technology Shenzhen Co., Ltd, Shenzhen 518172, China*
[3]*ShenLanZhongXin Technology Co., Ltd, Shenzhen 518172, China*

(Manuscript Received August 27, 2018; Revised April 30, 2019; Accepted May 6, 2019)

Abstract

This study designs and optimizes a high-loaded transonic fan stage using a curvature control method. A fan stage with a total pressure ratio of 2.49 and adiabatic efficiency of over 87 % at the design point is obtained after 3D optimizations. The geometric curvature of the blade passage has important driving and adjusting effects on the mainstream and on the flow in the boundary layer. The reasonable optimization of camber line curvature can weaken the radial secondary flow on the blade surface and decrease shock losses effectively. It can also postpone or suppress boundary layer separation by reorganizing aerodynamic load. Hence, secondary flow losses are reduced, and the overall stall margin is expanded. This method features high precision, high operability, and short design cycle, hence providing high-loaded fans/compressors with new freedom to improve design ability and offering new possibility to design system development.

Keywords: Aerodynamic optimization design; High-loaded fan; Curvature control; Aerodynamic performance; Flow structure

1. Introduction

Researching and applying the core design method of compression systems have always been essential in developing high-performance aeroengine technology. As modern high-performance compression systems head toward a larger thrust–weight ratio and higher efficiency, the fan/compressor is required to have stronger flow capacity, higher stage pressure ratio and efficiency as well as wider stall margin under all operation conditions compared with the usual. However, excessive improvement of the stage aerodynamic load will cause technological bottlenecks, such as high Mach number at the rotor tip, intense adverse pressure gradient, and large separation of the boundary layer in the blade passage. For an effective heat-work conversion process under adverse pressure gradient, the driving and adjusting abilities of the stream tube in the 3D environment in the compressor blade passage must be properly controlled. Therefore, the aerodynamic design for advanced compression systems should consider multiple factors, such as the shock wave resulting from expansion/compression flow effect and the 3D boundary layer separation induced by intense shear transport of viscous flow.

After proposing the concept of multistage axial compressors, long-term development produced numerous compressor design methods and concepts. Wu [1] proposed the theory of S_1/S_2 stream surfaces in turbomachinery, which promoted the development of aeroengines and gas turbines greatly. Based on this theory, Novak [2] raised the streamline curvature method to solve the full radial equilibrium equation, and Marsh [3] proposed the matrix throughflow method in which the stream function is introduced. Considering the sweep blade, Deich et al. [4] proposed the theory of boundary-layer fluid radial migration. Subsequently, Wang et al. [5] further proposed the swept/twisted blade design theory, which is widely applied in turbomachinery design at present. GE Company conducted an experiment on the test piece of a two-stage fan, GESFAR, which applied a forward-swept first-stage rotor blade design and led to a 4 % increase in efficiency and 80 % improvement in the engine's capability to resist distortion [6]. Denton [7] investigated the effect of sweep/lean on performance and flow structures for transonic blades and found that sweep/lean significantly affects stall margin.

Early technologies had difficulty in comprehensively considering the influence of blade geometry and complex flow conditions on aerodynamic performance. With a deep understanding of flow mechanisms, advanced technologies synthesized with 3D aerodynamic effect have been developed gradually. Wennerstrom [8, 9] introduced blades with splitters into a high-loaded rotor design, which effectively suppressed

*Corresponding author. Tel.: +86 13104050781
E-mail address: chenhuanlong@163.com
† Recommended by Associate Editor Cheolung Cheong

flow separation induced by a large flow turning angle. Chen and Liu [10] adopted the splitter blade method to increase the pressure ratio and efficiency of a single-stage fan to 2.3 and 88 %, respectively. Kerrebrock et al. [11-13] applied the concept of aspirated compressors to the design of a single-stage fan at different tip triangle velocities, which improved the pressure ratio to 1.5, 2.0, and 3.5. Song and Liu [14] developed an optimization system for tandem cascades based on an adaptive particle swarm optimization and validated the method by optimizing two large-turning tandem cascades. Li et al. [15] and Yang et al. [16] proposed the underlying physics mechanism of compressor flow by vorticity dynamics and performed a diagnosis and optimal design of the axial compressors in the 3D viscous flow environment by focusing on the boundary vorticity flux.

Current research on the curvature control method for the turbomachinery blade design remains insufficient. Korakianitis [17-20] conducted a series of studies and concluded that slope-of-curvature discontinuities will lead to the local peak distribution of aerodynamic parameters, which might cause separation or undesirable loading distribution. Corral and Pastor [21] drew a similar conclusion when they studied the simplified 2D blade design. Therefore, blade profile should have the slope of the curvature continuous in 2D blade designs. Yi [22] also found that the variation in the first- and second-order derivatives of the airfoil profiles could result in fluctuations in airfoil aerodynamic performance. Hamakhan and Korakianitis [23] used the curvature control method to modify the leading-edge geometry smoothly, thereby removing the peak load on the suction surface and diffusion region on the pressure surface. Turner et al. [24-28] conducted numerous studies on the relationship between blade geometry and flow parameters. Integrating 3D CFD approaches, they presented a turbomachinery design and optimization system based on the curvature control method. Balasubramanian et al. [29] optimized the laminar flow airfoil of a horizontal axis wind turbine by modifying the geometric curvature of camber lines and obtained fine performance. Zhang et al. [30] proposed a leading-edge design method based on curvature control and reduced the dissipation losses of the leading edge to 2/3. Song and Gu [31] redesigned the leading edge of a transonic rotor via curvature continuous and improved the rotor blade's efficiency as well as stability. Chen et al. [32] conducted curvature control optimization and flow diagnosis on a 1.5-stage high-pressure compressor rotor and increased its stage efficiency by 1.668 %. Li et al. [33] proposed a cascade design method and proved its validity using 14 parameters.

The common objectives for using curvature control methods are to promote the uniformity of parameter distribution, optimize flow structures on the blade surface, and reduce the high-loss region with the curvature and the slope of the curvature continuous for 2D blade profiles. As such, high-efficiency and high throughflow turbomachinery designs can be obtained easily.

This study performed an aerodynamic design and optimization for a high-loaded transonic fan stage. Through deep analysis of design data and flow parameters, related rules among the geometric curvature, aerodynamic parameters, and flow structures were explored. The underlying dynamic and physical mechanisms of shock wave control as well as that of the boundary–layer flow separation control on the suction surface were discussed.

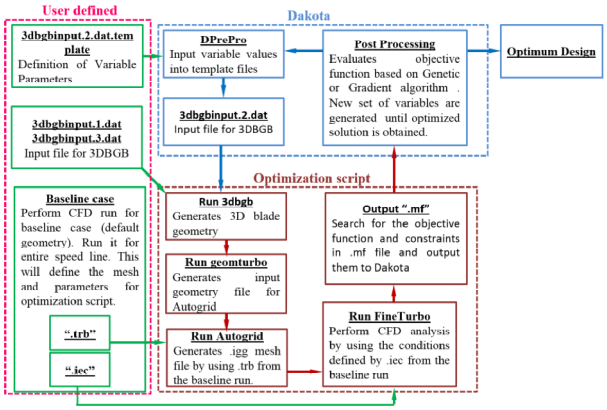

Fig. 1. Optimization system.

2. Optimization system

The aerodynamic optimization system applied in this study is shown in Fig. 1. This system operates on Shell script, Python script, and Fortran executable program in the Linux framework. It is divided into three parts: The user-defined, the optimization script, and the Dakota optimization modules [34].

The user-defined module completes the definition of geometric parameters and optimization variables, mesh generation, and boundary condition setting for CFD solver. After the preparation, the optimization script module executes the 3D blade geometry generator code of 3DBGB [35], thereby generating the 3D blade geometry and inputting corresponding files for the AutoGrid module. AutoGrid is the mesh generator of the CFD solver Fine/Turbo, which runs to obtain the objective function and transmit output files automatically after each iteration. The central work of the Dakota optimization module is to guide the optimization process and deliver parameters, including optimization variables, after each optimization. A single objective genetic algorithm and a gradient algorithm are utilized to obtain optimum results.

The curvature and the thickness of the camber line are defined with the cubic B-spline in the blade geometry generation system, which keeps the third derivative of interpolation nodes continuous and the curves smooth. This condition can avoid the undesirable aerodynamic impact introduced by interpolation discontinuous.

The adopted cubic B-spline function is defined as follows:

$$S_i(t) = \sum_{r=0}^{3} P_{i+r} B_r(t), \; t \in [0,1] \tag{1}$$

where P_{i+r} is the coordinate of control points for the i section of curve S_i; $B_t(t)$ is the spline basis function; and t is a parameter.

The mathematical definition of the cubic spline basis function is given as:

$$\begin{cases} B_0(t) = \left[-t^3 + 3t^2 - 3t + 1\right]/6 \\ B_1(t) = \left[3t^3 - 6t^2 + 4\right]/6 \\ B_2(t) = \left[-3t^3 + 3t^2 + 3t + 1\right]/6 \\ B_3(t) = t^3/6 \end{cases}. \quad (2)$$

In combination with parametric spline curves, 3D blade geometry is generated by directly controlling the curve, curvature, and slope of curvature of the camber line. Subsequently, the objective function can be fully optimized with the blade geometry. Moreover, this aerodynamic optimization system includes other advanced methods, such as the matching optimization of incidence angle and deviation angle, 3D sweep/lean optimization, and stacking optimization of blade sections, which gives the system an edge in the modern design and optimization of turbomachinery.

3. Numerical method and validation

Meshing and CFD simulations are performed using the NUMECA software [36]. The Navier–Stokes equation is used to solve 3D steady flow in the fan stage. In consideration of the accuracy and iteration time of the calculation, the second-order central difference scheme and an explicit four-stage Runge–Kutta scheme are used for spatial and time discretization, respectively. Multigrid and local time-stepping methods are adopted to accelerate convergence. The Spalart–Allmaras turbulence model is selected in consideration of its precise prediction and excellent numerical stability. As for boundary conditions, an absolute total temperature of 288.15 K and an absolute total pressure of 101325 Pa are given at the inlet plane of the calculation domain with the axial flow direction. At the outlet plane of calculation domain, the static pressure is ruled by simple radial equilibrium, which is given as 210000 Pa at the mean radius position at the design point. No-slip and adiabatic wall conditions are used for all wall boundaries. Additionally, the computational domain is divided into two parts: the rotor and the stator. The rotor blade speed in the rotor part is 21500 rpm, and the casing is stationary. The mixing plane approach [36] is used at the rotor/stator interface.

Full 3D steady simulation is performed. The fluid is considered ideal air. The governing equation [36] is the Reynolds-averaged Navier–Stokes (RANS) equations for the relative velocities in the rotating frame of reference, which can be expressed as:

$$\frac{\partial \vec{U}}{\partial t} + \nabla \cdot \vec{F}_I + \nabla \cdot \vec{F}_V = Q \quad (3)$$

Table 1. Grid independence confirmation.

Cases	Total grid cell number	Performance parameters		
		Efficiency η	Pressure ratio π	Mass flow rate $\dot{m}$ (kg/s)
1	1097836	85.35 %	2.467	25.114
2	1328856	85.39 %	2.467	25.099
3	1401132	85.39 %	2.466	25.097

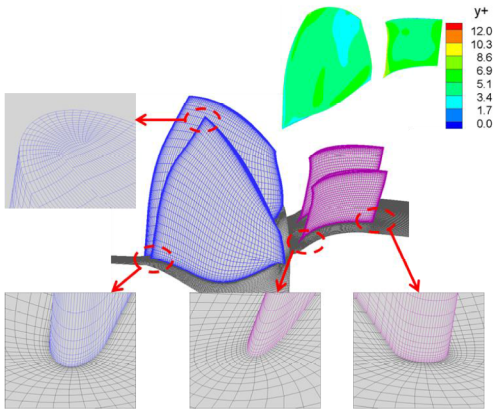

Fig. 2. Geometry, mesh, and y^+ on the blade surface.

where $\vec{U}$ is the vector of the conservative variables; $\vec{F}_I$ is inviscid flux vector; and $\vec{F}_V$ is viscous flux vector. Their variable forms are given by:

$$\vec{U} = \begin{bmatrix} \overline{\rho} \\ \overline{\rho}\tilde{w}_1 \\ \overline{\rho}\tilde{w}_2 \\ \overline{\rho}\tilde{w}_3 \\ \overline{\rho}\tilde{E} \end{bmatrix} F_{Ii} = \begin{bmatrix} \overline{\rho}\tilde{w}_i \\ \overline{p^*}\delta_{1i} + \overline{\rho}\tilde{w}_i\tilde{w}_1 \\ \overline{p^*}\delta_{2i} + \overline{\rho}\tilde{w}_i\tilde{w}_2 \\ \overline{p^*}\delta_{3i} + \overline{\rho}\tilde{w}_i\tilde{w}_3 \\ (\overline{\rho}\tilde{E} + \overline{p^*})\tilde{w}_i \end{bmatrix} -F_{Vi} = \begin{bmatrix} 0 \\ \overline{\tau}_{i1} \\ \overline{\tau}_{i2} \\ \overline{\tau}_{i3} \\ \overline{q}_i + \tilde{w}_i\overline{\tau}_{ij} \end{bmatrix} \quad (4)$$

where the superscripts "-" and "~" are the time average value and density weighted average value, respectively; w_i is the x_i component of the relative velocity; E is the total energy; p^* is the total pressure; δ_{ij} is the Kronecker number; τ_{ij} is the Reynolds stress; and q_i is the heat flux component.

The contributions of the Coriolis and centrifugal forces are contained in the source item vector Q, which is given by:

$$Q = \begin{bmatrix} 0 \\ (-\overline{\rho})[2\vec{\omega} \times \vec{w} + (\vec{\omega} \times (\vec{\omega} \times \vec{r}))] \\ \overline{\rho}\vec{w}\nabla(\frac{1}{2}\omega^2 r^2) \end{bmatrix} \quad (5)$$

where ω is the angular velocity of the relative frame of reference; r is the radius; and $\vec{w}$ is the relative velocity.

The geometry, mesh, and y^+ distribution on the blade surface are observed in Fig. 2. Mesh generation is finished by the AutoGrid5 module. All blades are meshed using the O_4H grid

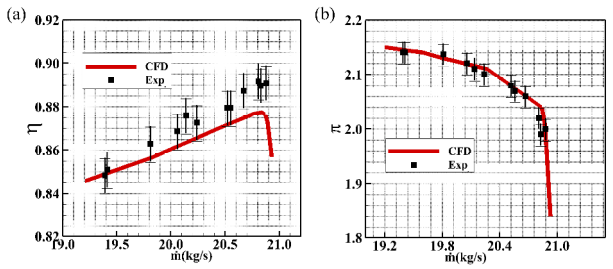

Fig. 3. Aerodynamic performance map for the NASA Rotor 37: (a) Adiabatic efficiency vs. mass flow rate; (b) total pressure ratio vs. mass flow rate.

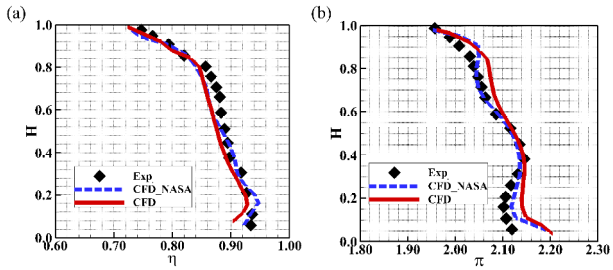

Fig. 4. Aerodynamic performance comparison for the NASA Rotor 37: (a) Adiabatic efficiency distribution; (b) total pressure ratio distribution.

technology. For an optimal mesh resolution, a grid independence study is conducted for the baseline. As presented in Table 1, the relative variation of mass flow rates is no more than 0.1 % when the total grid cell number exceeds 1320000. Hence, the number around 1320000 for the total grid cell number is selected for further investigation. Moreover, the y^+ distribution on the wall is less than 10 for the capture of flow information in the boundary layer near the wall.

Experimental data of the NASA Rotor 37 are used to verify the validity and reliability of the simulation. The NASA Rotor 37 is used for the ASME/IGTI "blind test case" to demonstrate how various codes lead to different results [37]. Its test data have been used as a benchmark for many 3D RANS solvers of turbomachinery in the past 20 years. As shown in Fig. 3, the performance maps are given with the standard condition and rotor blade design speed of 17188.7 rpm. The comparison between the simulation and experimental data and errors is also displayed in Fig. 3. The total pressure obtained by the simulation agrees well with the experimental data, whereas the forecast of efficiency is smaller than that of the experimental data. Nevertheless, the trend of the efficiency deviation is correct, and its values are within the error band, whereas the peak point of the efficiency deviation is 1 % or so. The errors are within the allowable range. Thus, the numerical method used in this study is valid and reliable [38, 39]. Bruna and Turner [40] compared the CFD result with the experimental data of the NASA Rotor 37. Fig. 4 shows the distribution of the adiabatic efficiency and the total pressure ratio of the NASA Rotor 37. The curve denoted as CFD in Fig. 4 corresponds to the simulation results in Fig. 3, and the data of the other curves, which are denoted as CFD_NASA and Exp., can be referred from the report [40]. The curve denoted as CFD_NASA is the simulation result by NASA, and the curve denoted as Exp. is the experimental data of the NASA Rotor 37. As shown in Fig. 4, the computed result of adiabatic efficiency matches the experimental data well despite underestimating the measurement between 50 % and 85 % span sections. Additionally, the total pressure ratio is predicted well for overall spans, whereas CFD overestimates the data below 15 % span section. This research [40] ensures the accuracy and validity of the CFD method in this study.

Table 2. Design parameters of the transonic fan stage.

Design parameters	Values
Corrected first rotor tip tangent speed (m/s)	495.32
Corrected design angular velocity (rpm)	21500.0
Design flow rate (kg/s)	25.5
Stage tip flow coefficient	0.356
Stage tip work coefficient	0.517
Hub/tip ratio at the inlet of rotor	0.336
The number of blades for rotor and stator	14/34
Clearance at rotor tip (mm)	0.5

Table 3. 1D design result.

Performance parameters	Values
Total pressure ratio π	2.4633
Total temperature ratio τ	1.3175
Adiabatic efficiency η	0.9252

4. 1D and Q-3D designs

4.1 1D design

The 1D design method is adopted on the basis of the mean radius, and the quasi-three-dimensional (Q-3D) method, T-AXI [41, 42], is used. These methods provide related initial aerodynamic and geometric data to the subsequent 3D design and optimize curvature control [26].

The 1D design is a vital stage for the overall fan/compressor design process. With the design indicators set by the initial design, it uses the aerodynamic and geometric parameters at the mean radius to calculate and obtain the original geometry data at the meridian plane of the fan stage. Table 2 lists the design parameters of the high-loaded transonic fan. In comparison with fans of the same type, the fan designed in this study has higher aerodynamic performance indicators; thus, it has more technological difficulties in terms of aerodynamic design.

Results of the 1D design are shown in Table 3. Some critical flow losses, such as secondary flow and shock losses, are ignored in the 1D design. Hence, the performance, whose total pressure ratio of the fan stage is more than 2.46 and adiabatic efficiency is more than 92 %, is much higher than real condi-

Table 4. Parameters of the Q-3D design result.

Performance parameters	Values
Total pressure ratio π	2.4540
Total temperature ratio τ	1.3215
Adiabatic efficiency η	0.9094

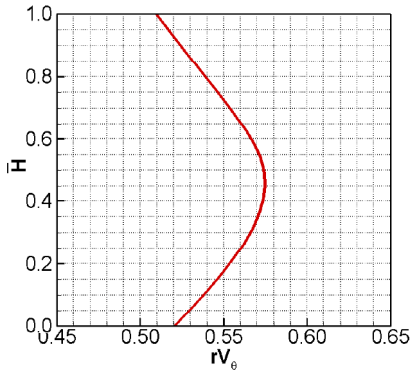

Fig. 5. Angular momentum distribution of the rotor outlet.

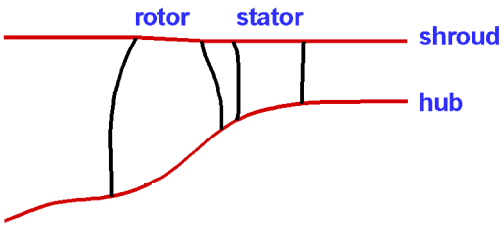

Fig. 6. Hub and shroud profiles.

tions. This problem will be amended in subsequent Q-3D and 3D designs by adding complex flow effect.

4.2 Q-3D design

The Q-3D through-flow design of the transonic fan stage is conducted on the basis of the iteration method of the stream tube [41, 42] to analyze further the detailed parameters of the fan stage and confirm the indicators acquired by the 1D design. The performance parameters of the design result are listed in Table 4. Integrated with relevant loss models, the design result is selected from numerous design cases with proper angular momentum distribution and suitable profiles of hub and shroud. The efficiency of the designed fan is still more than 90 %, whereas the pressure ratio remains 2.45.

The angular momentum distribution at the outlet of the rotor is shown in Fig. 5. Similar to that of a parabola, the regulation applied is bigger in the middle but smaller on both sides. This type of regulation has two purposes: (1) Use the pressure-rise and work-doing capability in the middle section sufficiently and (2) ensure good manufacturability of the fan rotor blade to some extent.

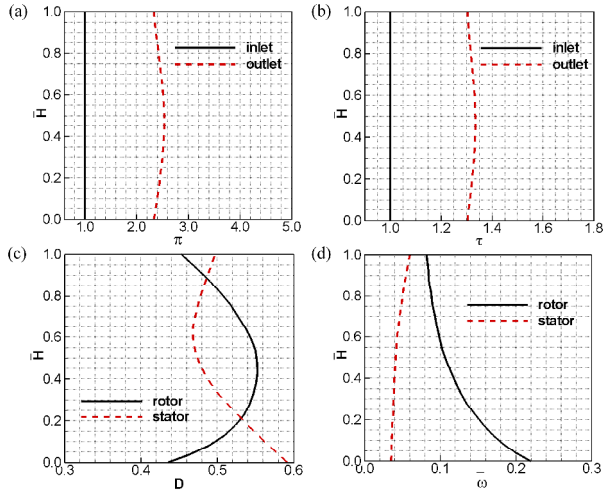

Fig. 7. Aerodynamic parameter distribution of the blade passage: (a) Stage total pressure ratio; (b) stage total temperature ratio; (c) diffusion factor; (d) total pressure loss coefficient.

The hub and shroud profiles in the meridian plane are depicted in Fig. 6. In the flow region of the blade passage, the shroud profile has a concave curve followed by the convex curve, whereas the hub profile shrinks gradually. This type of design is beneficial for driving and adjusting the flow of the stream tube for the high-loaded fan as well as converting heat to work efficiently.

The aerodynamic parameter distribution in the blade passage is further presented in Fig. 7. In terms of the Q-3D design and analysis, the designed fan stage is found to have good performance on pressure rise. Moreover, its diffusion factor distribution as well as its level of aerodynamic losses coincide with the rules that are already understood about transonic fans.

5. 3D optimization

5.1 3D design

The Q-3D design can rapidly acquire results, especially for numerous systematic works, such as the through-flow design of multistage turbomachinery and the selection of preliminary designs. The 3D design cannot match this merit. However, the Q-3D design cannot consider real blade structures and factors, such as corresponding 3D shock wave and boundary layer separation, which seriously constrain the aerodynamic performance of transonic fans. Consequently, the 3D flow must be diagnosed, and the designed fan must be optimized to confirm further and validate the aerodynamic performance of the high-loaded transonic fan.

Based on the 1D and Q-3D designs above, the 3D blade geometry generator 3DBGB in the optimization system operates to generate the geometric structure of the blade passage. The design result is regarded as the initial case for the optimization and is denoted as baseline in the following text. The blade geometry that provides basic data for the subsequent aerodynamic optimization is shown in Fig. 2.

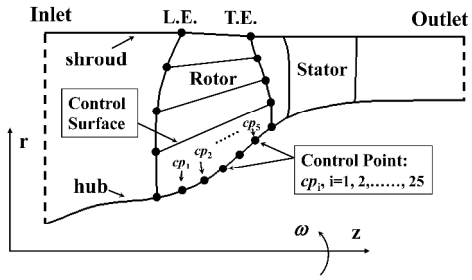

Fig. 8. Computational domain and control points for rotor blade optimization.

5.2 Optimization model and method

Fig. 2 shows the geometry, mesh, and y^+ distribution on the blade surface for the fan stage. The total grid cell number exceeds 1320000 for the whole stage, and the y^+ of the first grid cell is less than 10 to capture the flow details in boundary-layer areas. Besides, buttressed by the geometric structure of the initial case (denoted as baseline), the parametric design method is applied to parameterize blade geometry and further provide information of variables for overall 3D optimizations.

The optimization statements are as follows:

Maximize: Adiabatic efficiency η on the highest efficiency point for fan stage.

η can be defined as $\eta = f(cp_1, cp_2, \ldots\ldots, cp_{25})$, in which cp_1, cp_2, ……,cp_{25} are control points for design variables.

Constraints: Mass flux $\dot{m} \geq \dot{m}_0$ (baseline); total pressure ratio $\pi \geq \pi_0$ (baseline);

Design variables: A total of 25 variables for five sections, which have four points at each section to control curvature for the unit chord and one point to control the position of the maximum thickness point, which are shown in Figs. 8 and 14;

Genetic algorithm parameters: Population size of 50 and maximum iteration of 150;

Gradient algorithm parameters: Maximum iteration of 300, and the initial variables for computing gradient are the variables from the optimum result computed by the genetic algorithm;

Constants: Use blade definitions from the 3D design.

Optimization processes include two steps. First is the optimization of rotor camber line (denoted as opt_rotor), which only optimizes the rotor. Then, by keeping the optimized rotor geometry, the stator camber line is also optimized (denoted as opt_rotor&stator) as the second step. The case opt_rotor& stator is the optimum case and is thus denoted as optimum in the following text. The overall optimization processes are conducted within the stage-flow environment to ensure that the data at the interface between rotor and stator blades can reflect the substance of physical flow accurately.

Fig. 8 depicts the computational domain and shows the control points and control surfaces for the rotor blade optimization. The selection of control points for the stator blade optimization is similar to what is shown in Fig. 8.

During practical operations, genetic algorithm searches for all possible objective directions quickly and widely through global optimization. Gradient algorithm usually spends much time on calculation, but it can find the optimal solution for objective functions precisely. Therefore, in this study, the purpose of using gradient algorithm based on the scheme given by the genetic algorithm is to shorten calculation time and promote the result effectively. After each optimization, diagnoses and analyses of flow structures are performed to determine the next work direction.

Table 5. Performance comparison of different design cases.

Cases	Efficiency η		Total pressure ratio π		Mass flow rate $\dot{m}$ (kg/s)	
	Values	(%)	Values	(%)	Values	(%)
Baseline	85.39 %	0.0	2.467	0.0	25.10	0.0
Opt_rotor	87.50 %	+2.47	2.489	+0.89	25.81	+2.83
Opt_rotor&stator	87.50 %	+2.47	2.490	+0.93	25.80	+2.79

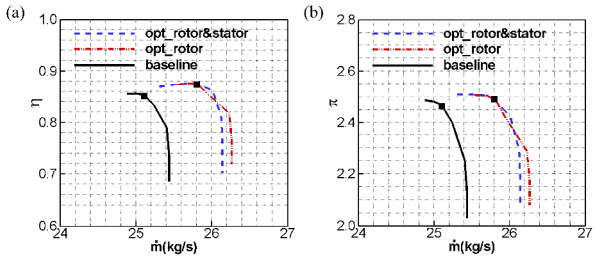

Fig. 9. Aerodynamic performance map of the fan stage: (a) Adiabatic efficiency vs. mass flow rate; (b) total pressure ratio vs. mass flow rate.

5.3 Geometry and performance analysis

The comparison of aerodynamic performance for the fan stage is given in Table 5. The aerodynamic performance at the design point has been improved to varying degrees with curvature control optimizations on airfoil camber lines. Adiabatic efficiency increases by 2.47 %. Pressure ratio increases by 0.89 % and 0.93 %, whereas mass flow rate increases by 2.83 % and 2.79 % for the opt_rotor and opt_rotor&stator cases, respectively. Synthesized with the distribution of the fan-stage map as shown in Fig. 9, the promotion of the aerodynamic performance through optimization is revealed clearly. Results in Fig. 9 show that in contrast to the opt_rotor case, the stage blockage mass flow rate of the opt_rotor&stator case decreases, but its stall mass flow rate increases, and its high-efficiency region also widens. These results illustrate the validity and importance of the curvature control method.

The spanwise distribution of efficiency and pressure ratio at the design point are shown in Figs. 10 and 11. Through optimization, the efficiency and pressure ratio between 50 % span and 70 % span increases. Thus, work capability above 50 % span is utilized sufficiently, which contributes to the improvement of overall fan-stage aerodynamic performance. Specific discussions and analyses of the flow control mecha-

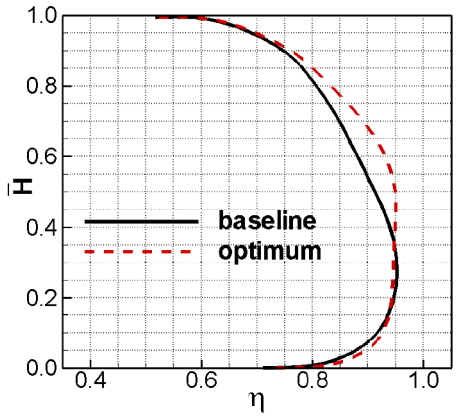

Fig. 10. Adiabatic efficiency vs. relative blade height.

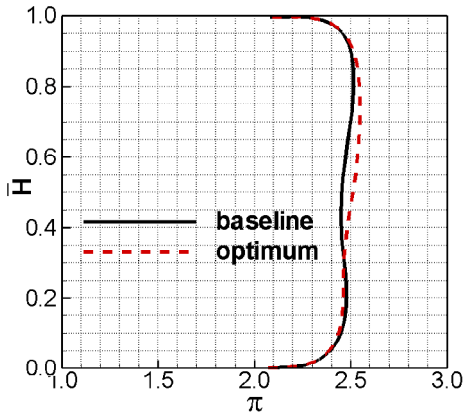

Fig. 11. Total pressure ratio vs. relative blade height.

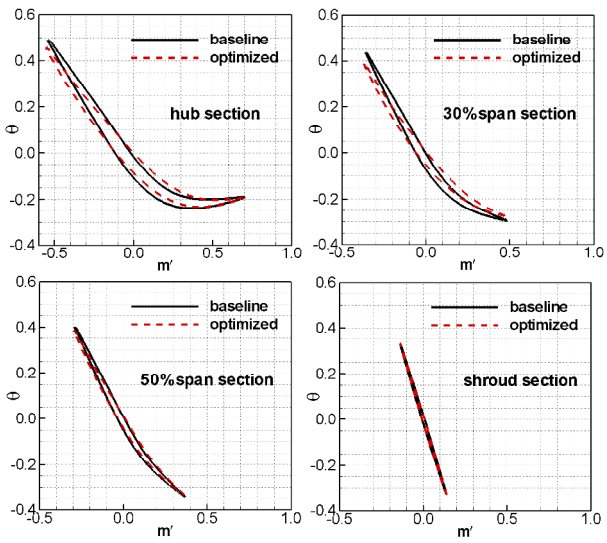

Fig. 12. Rotor blade profiles for the baseline and opt_rotor cases.

nism are described in the following context.

The reason for the change of aerodynamic performance can be understood clearly by further analyzing the blade passage geometry. Fig. 12 compares the rotor blade shapes before and after optimization. Curvature control decreases camber angles

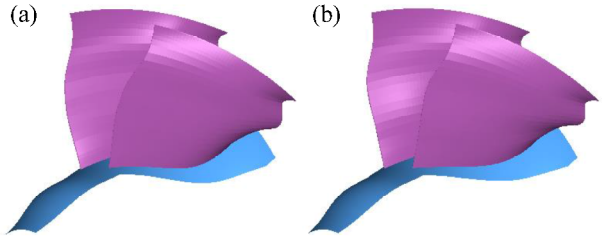

Fig. 13. Comparison of rotor 3D configurations: (a) Baseline; (b) opt_rotor&stator.

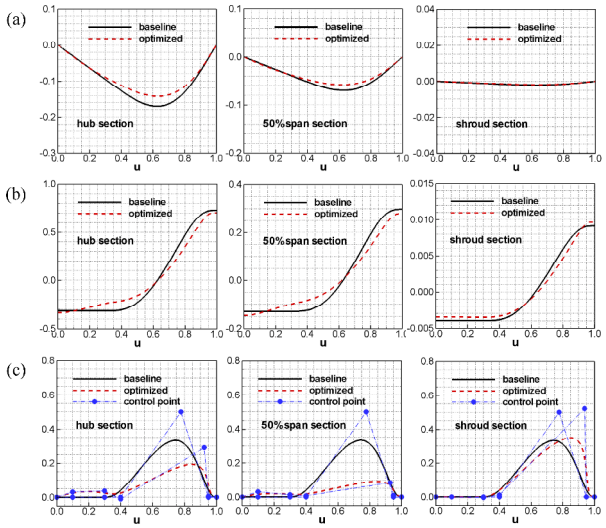

Fig. 14. Curve, slope and curvature of rotor profile camber lines: (a) Curve; (b) slope of curve; (c) curvature.

at almost overall spanwise sections, especially below the 50 % span, and the location of maximum deflection is closer to the trailing edge of corresponding profiles, whose mechanism resembles an aft-loaded airfoil in turbine designs. This condition is consistent with the fundamentals of the flow rules of transonic rotor profiles. Projecting the profiles to the stream surface as in Fig. 12 will acquire 3D airfoils. Then, stacking all the 3D airfoils at their center of gravity can further obtain 3D blade configurations, as shown in Fig. 13. In combination with the result shown in Fig. 12, although geometric projections of the special curves in the meridian plane for the blade leading edge are identical before and after optimization, curvature control can still modify the spatial curve of the 3D blade leading edge by modifying the axial-section component of the camber line curvature of blade profiles. As such, it can further change the shock wave structure at the leading edge. Meanwhile, by improving the physical match between geometry and aerodynamics, this modification enhances shock wave control and captures the capability of 3D blades. Consequently, the driving and adjusting effect on the stream tube in blade passages is acquired efficiently.

Different from the distinct characteristics indicated by performance parameters and blade geometry, curvature, a

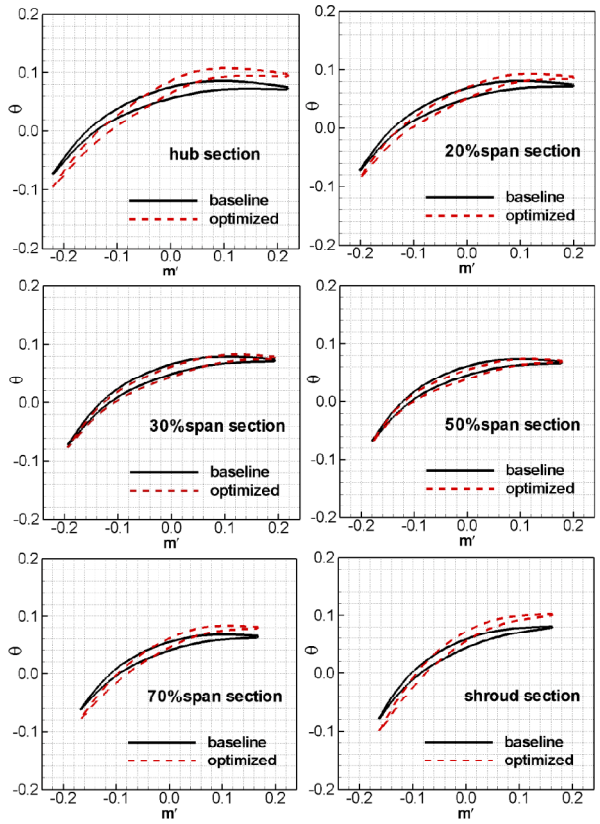

Fig. 15. Stator blade profiles for the baseline and opt_rotor&stator cases.

mathematical parameter, usually reveals the mechanism of the capture for 3D spatial shock wave by blades and that of the driving and adjusting effect on passage flow implicitly. Fig. 14 presents the distribution of curve, slope, and curvature for rotor profile camber lines. Results show that the maximum deflection of the rotor is reduced, and its location moves downstream with optimization. Simultaneously, the subsonic and transonic profiles and the camber line curvature of their forepart cannot be zero, because it is beneficial for the acceleration of subsonic/transonic flow and compensates the radial velocity imbalance for supersonic incoming-flow sections to some extent.

In a real flow environment, flow conditions in the rotor blade passage influence the flow structure in the downstream stator blade passage directly. Consequently, the stator blade passage must be optimized based on the optimized rotor blade geometry.

Stator blade shapes before and after optimization are shown in Fig. 15. At the hub section, the location of maximum deflection is closer to the trailing edge compared with the baseline case. This supersonic feature of the hub blade profile is due to the essential characteristic of high-loaded transonic fans, in which rotor and stator blade passages are transonic. Thus, the hub section of the stator blade remains supersonic, resulting in a supersonic feature of corresponding blade profiles. According to Fig. 15, the maximum deflection between 30 % span and 50 % span decreases, and the stagger angle from the 70 % span to the shroud section increases. Finally, to drive and adjust fluid flow effectively, the high-loaded transonic stator blade passage has a highly 3D individualized feature (shown as Fig. 16), which is similar to the rotor blade passage. This result also shows that the curvature control method can operate as an effective technological approach to achieve 3D individualized design for blade geometry.

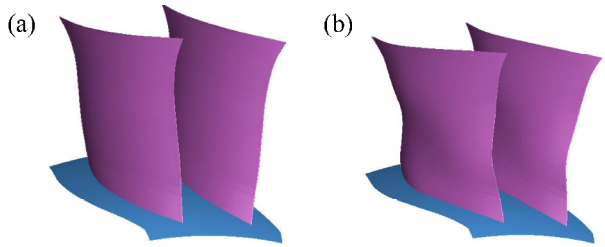

Fig. 16. Comparison of stator 3D configurations: (a) Baseline; (b) opt_rotor&stator.

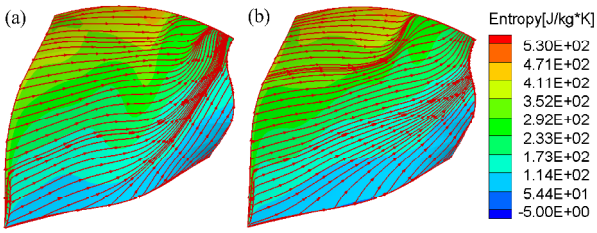

Fig. 17. Entropy and skin-friction lines on the suction surface of the rotor blade: (a) Baseline; (b) opt_rotor&stator.

5.4 Flow checking and analysis for fan stage

The change of the geometric structure inevitably affects the distribution rule of aerodynamic parameters in the flow passage and further influences the aerodynamic performance of the overall fan stage. To confirm flow condition, Fig. 17 presents the skin-friction lines and the distribution of entropy on the suction surface of the rotor blade. The variation of curvature can reorganize the distribution feature of entropy and the structure of the secondary flow. The curvature control motivates the relocation of the shock wave and weakens its strength on the suction surface; thus, shock losses are reduced remarkably. Meanwhile, reasonable curvature distribution apparently lowers the scale and intensity of the secondary flow in the boundary layer, thereby avoiding the production of high entropy in an extensive area. Thus, the aerodynamic performance of the rotor blade passage is improved.

The isentropic Mach number on the rotor blade surface as depicted in Fig. 18 can further explain that the optimized rotor blade reduces the intensity of the shock wave and shrinks the flow region of the high Mach number. Primarily, the peak value of the relative Mach number and the streamwise fluctuation decreases. These changes improve the interaction between the shock wave and the boundary layer effectively. The optimized rotor blade reflects the original design intent of

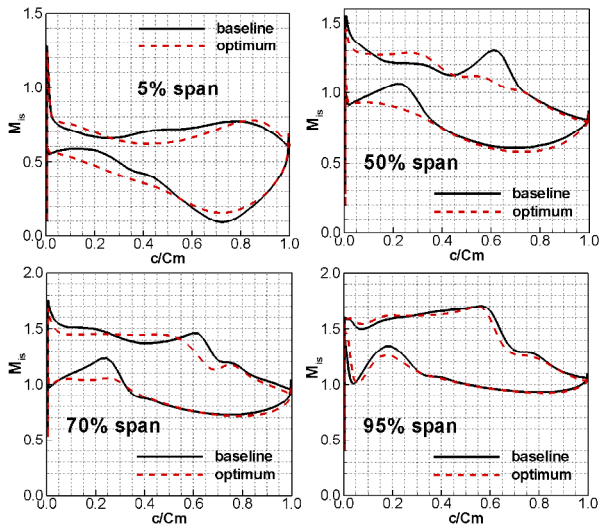

Fig. 18. Isentropic Mach number on the surface of the rotor blade.

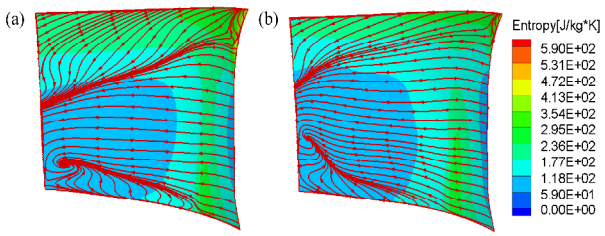

Fig. 19. Entropy and skin-friction lines on the suction surface of the stator blade: (a) Baseline; (b) opt_rotor&stator.

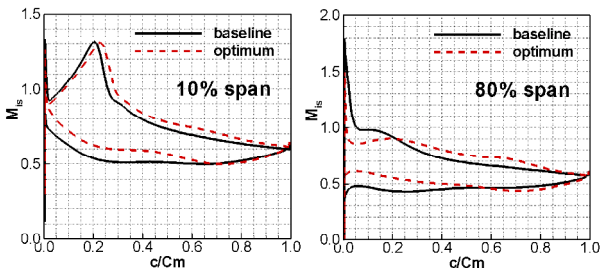

Fig. 20. Isentropic Mach number on the surface of the stator blade.

transonic compressor intensively. It utilizes the pressure-rise effect and lowers shock losses down to a reasonable level.

Fig. 19 presents the distribution of entropy and skin-friction lines on the suction surface of the stator blade. Results show that the high-entropy region on the suction surface decreases, whereas the scale and intensity of the corner separation and that of the secondary flow are lowered. These outcomes improve the through-flow capability and expand the stability of the stator blade passage and even the overall fan stage. However, the separation in the lower corner area has not been controlled thoroughly. It may be relevant to the large camber angle of the lower half of the stator spanwise sections and has become one of the most important issues to be solved in the next research.

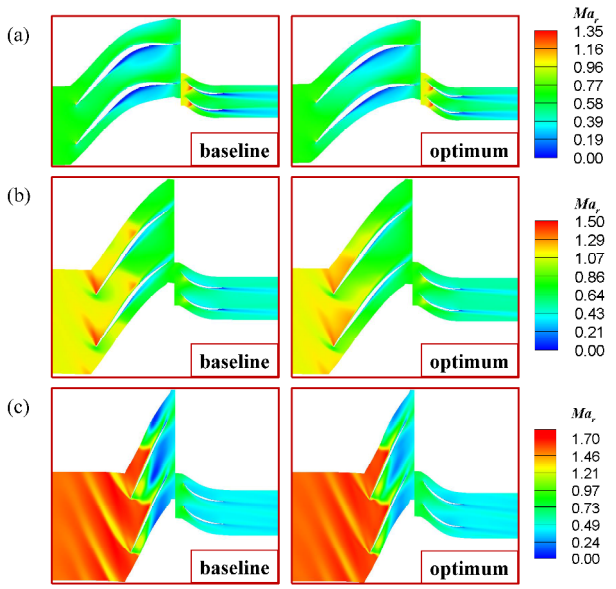

Fig. 21. Relative Mach number in the blade-to-blade section: (a) 5 % span section; (b) 50 % span section; (c) 95 % span section.

The isentropic Mach number on the stator blade surface is given in Fig. 20. With optimization, the peak value of the Mach number at the leading edge decreases to varying degrees except that of the midspan section, whereas the location of the Mach number with peak value moves downstream for the sections from hub to 50 % spans. This result is due to the wide stability of the fan stage.

To observe the flow structure in the blade passage distinctly, Fig. 21 shows the relative Mach number at 5 %, 50 %, and 95 % spans for the blade-to-blade section of the fan stage. The characteristics of driving and adjusting flow have been improved, especially near the endwall. At majority of the spanwise sections, low velocity regions on the blade surface and that in the wake are declined. Meanwhile, at the leading edge, the strength of the shock wave near the midspan degrades. Additionally, the change of the flow at the rotor tip section remains small, which can be because few geometry changes have taken place for the rotor tip after optimization, as illustrated in Fig. 12. The problems of how to control the curvature distribution of blade surfaces directly, how to decrease the low-velocity region near the surface of the rotor blade passage further, and how to reduce the intensity of shock wave around the rotor tip may become the imperative questions that will guide future research.

The fundamental theories of the turbomachinery compression system design state that raising rotor speed and increasing flow turning angles are the two main approaches for improving the unit aerodynamic loading of fan stages. The spanwise distribution of the flow angles at the inlet and outlet planes of rotor and stator blades is given in Fig. 22. Clearly, the stator blade passage has large turning angles for overall spanwise

Table 6. Stall margin for design and off-design conditions.

Rotating speed	Baseline	Opt_rotor&stator	Increased percentage
100 %n	10.40 %	10.79 %	+0.39 %
90 %n	13.71 %	10.03 %	−3.68 %
110 %n	14.30 %	12.50 %	−1.80 %

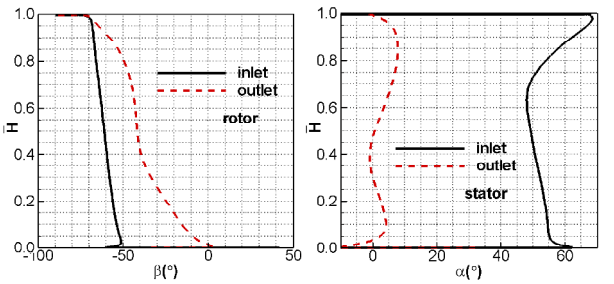

Fig. 22. Flow angle for the fan stage.

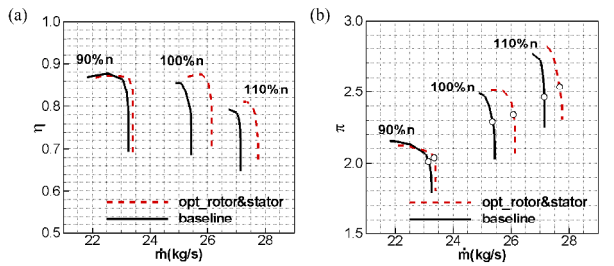

Fig. 23. Aerodynamic performance map for the fan stage: (a) Adiabatic efficiency vs. mass flow rate; (b) total pressure ratio vs. mass flow rate.

sections. Particularly, the maximum turning angle of the stator blade should be more than 60 degrees and is located at the hub section to satisfy the requirement of high stage total pressure ratio.

Finally, off-design performance reveals implicit problems and shows the basic direction for the next optimization. The performance map and the stall margin at three different speeds are shown in Fig. 23 and Table 6, respectively, to investigate the performance of the designed and optimized high-loaded transonic fan stage under variable conditions. The stall margin is defined by:

$$SM = \left(\frac{\pi_{Ks}^{*} / m_{as}}{\pi_{K0}^{*} / m_{a0}} - 1 \right) \times 100\ \% \tag{6}$$

where π_{Ks}^{*} and m_{as} are the total pressure ratio and mass flux at the stall boundary, respectively; π_{K0}^{*} and m_{a0} are the total pressure ratio and mass flux at the design point of the compressor, respectively. The stall mass flow rate of the fan stage increases at design speed after optimization, while the pressure ratio and adiabatic efficiency rise as well. Results in Table 6 show that the range of stability increases to some extent at the design condition but declines at 90 % and 110 % rotating speeds. Thus, in contrast to general fan designs, especially those with a total pressure ratio of around 2.0, the high-pressure-ratio design in this study sacrifices some stall margins to obtain high design performance before the off-design-point optimization is conducted. However, results of the geometry and flow structure analyses show that the curvature control method can absolutely change flow conditions and improve aerodynamic performance efficiently. Thus, the stall margin at off-design conditions may still be improved when multipoint optimization is finished. The study for the design and optimization of the high-loaded fan through curvature control has obtained partial results in terms of further exploring the potentials of overall aerodynamic performance improvement. Overall, the curvature control method should undergo further scrutiny to expand the aerodynamic design system of turbomachinery.

6. Conclusions

This study presented the design and optimization of a single-stage high-loaded axial transonic fan based on a curvature control method and performed internal flow diagnoses. Buttressed by viscous 3D CFD technologies, detailed flow data and performance parameters were obtained to analyze the association rules among the geometric curvature of the blade passage, aerodynamic performance parameters, and transonic flow structures. The mathematical and physical relationships between geometric curvature and fluid dynamics were analyzed to discuss the underlying dynamics and physical mechanisms of the shock wave control and its application to the transonic passage as well as that of the boundary-layer flow separation control with geometric curvature control near the wall.

To ensure continuous geometric curvature, camber line curvature control can adjust the secondary flow in the boundary layer near the wall. Meanwhile, it can reconstruct the structure of the shock wave and reorganize the streamwise pressure gradient. By weakening the scale and strength of the boundary layer separation and improving the uniformity of aerodynamic parameter distribution, this method can cut down the flow losses in diffused blade passage and influence the range of stability. With vital technological connotation and physical meaning, it deserves to be studied deeply as a considerably advanced method to supplement the aerodynamic fan/compressor design.

In a 3D stage viscous-flow environment, the total pressure and mass flow rate of the optimal fan case after curvature optimization reached 2.49 and 25.8 kg/s, respectively, whereas the adiabatic efficiency was more than 87 %. This result not only satisfied initial design indicators but also presented higher aerodynamic performance compared with fans of the same type.

The rotor and stator in the high-loaded transonic fan stage

are all transonic; thus, the design demand of large stage total pressure ratio normally leads to large flow turning angles at the hub section of the rotor blade and at overall spanwise sections of the stator blade, which is often close to and even more than 60 degrees. This measurement increases the possibility of large-scale boundary layer separation induced by intense adverse pressure gradient. Therefore, adjusting geometric curvature distribution reasonably can weaken the internal secondary flow of blade passage. As a result, the high-throughflow capability of the whole fan stage is improved effectively.

Acknowledgments

This work was supported by the National Natural Science Foundation of China (Grant Number 51506036) and the small/micro enterprises entrepreneurship projects in science and technology of Shenzhen City, China.

Nomenclature

p	: Pressure, Pa
$\dot{m}$	: Mass flow rate, kg/s
rV_θ	: Non-dimensional angular momentum at the rotor outlet
$\bar{H}$	: Relative blade height, $(r\text{-}r_h)/(r_t\text{-}r_h)$
D	: Diffusion factor
m'	: Normal coordinate for the streamline
u	: Non-dimensional coordinate in basic airfoil plane
c	: Local meridian curve distance, m
C_m	: Total meridian curve distance, m
M or Ma	: Mach number
n	: Rotating speed, rpm

Greek

ρ	: Density, kg/m^3
η	: Efficiency
π	: Pressure ratio
τ	: Temperature ratio
$\bar{\omega}$	: Total pressure loss coefficient
θ	: Circumferential coordinates
α	: Absolute flow angle, degree
β	: Relative flow angle, degree

Subscripts

is	: Isentropic
r	: Relative conditions
t	: Tip
h	: Hub

Abbreviation

L.E.	: Leading edge
T.E.	: Trailing edge

References

[1] C. H. Wu, A general theory of three-dimensional flow in subsonic and supersonic turbomachines of axial-, radial-, and mixed-flow types, *NASA Report No. NACA-TN-2604* (1952).

[2] R. A. Novak. Streamline curvature computing procedures for fluid flow problems, *Journal of Engineering for Gas Turbines and Power*, 89 (4) (1967) 478-490.

[3] H. Marsh, A digital computer program for the through-flow fluid mechanics in an arbitrary turbomachine using a matrix method, *Aeronautical Research Council R & M No. 3509,* London: Her Majesty's Stationery Office Ministry of Council (1968).

[4] M. E. Deich, A. B. Gubalev, G. A. Filippov and Z. Q. Wang, A new method of profiling the guide vane cascade of stage with small ratios diameter to length, *Teplienergetika*, 8 (8) (1962) 42-46.

[5] Z. Q. Wang, S. K. Lai and W. Y. Xu, Aerodynamic calculation of turbine stator cascades with curvilinear leaned blades and some experimental results, *Proceedings of ISABE Conference*, Bangalore, India (1981).

[6] S. W. Kandebo, General electric tests forward swept fan technology, *Aviation Week & Space Technology*, 145 (13) (1996) 32.

[7] J. D. Denton and L. Xu, The effects of lean and sweep on transonic fan performance, *ASME Turbo Expo 2002: Power for Land, Sea, and Air*, Amsterdam, The Netherlands (2002) 23-32.

[8] A. J. Wennerstrom and G. R. Frost, Design of a rotor incorporating splitter vanes for a high pressure ratio supersonic axial compressor stage, *Report No. ARL-74-TR-0110,* Aerospace Research Labs Wright-Patterson AFB OH (1974).

[9] A. J. Wennerstrom, W. A. Buzzell and R. D. Derose, Test of a supersonic axial compressor stage incorporating splitter vanes in the rotor, *Report No. ARL-75-TR-0165,* Aerospace Research Labs Wright-Patterson AFB OH (1995).

[10] M. Z. Chen and B. J. Liu, Some progress in basic research and engineering development of compressor in China, *Aeroengine*, 33 (1) (2007) 1-9 (in Chinese).

[11] J. L. Kerrebrock, M. Drela, A. A. Merchant and B. J. Schuler, A family of designs for aspirated compressors, *ASME 1998 International Gas Turbine and Aeroengine Congress and Exhibition*, Stockholm, Sweden (1998) V001T01A051-1-11.

[12] B. J. Schuler, J. L. Kerrebrock, A. A. Merchant, M. Drela and J. Adamczyk, Design, analysis, fabrication and test of an aspirated fan stage, *ASME Turbo Expo 2000: Power for Land, Sea, and Air*, Munich, Germany (2000) V001T03 A102-1-6.

[13] A. A. Merchant, M. Drela, J. L. Kerrebrock, J. J. Adamczyk and M. Celestina, Aerodynamic design and analysis of a high pressure ratio aspirated compressor stage,

ASME Turbo Expo 2000: Power for Land, Sea, and Air, Munich, Germany (2000) V001T03A103-1-10.

[14] Z. Y. Song and B. Liu, Optimization design for tandem cascades of compressors based on adaptive particle swarm optimization, *Engineering Applications of Computational Fluid Mechanics*, 12 (1) (2018) 535-552.

[15] Q. Li, H. Wu, M. Guo and J. Wu, Vorticity dynamics in axial compressor flow diagnosis and design—Part II: Methodology and application of boundary vorticity flux, *Journal of Fluids Engineering*, 132 (1) (2009) 011102-1-12.

[16] Y. Yang, H. Wu, Q. Li, S. Zhou and J. Wu, Vorticity dynamics in axial compressor flow diagnosis and design, *Journal of Fluids Engineering*, 130 (4) (2008) 041102-1-9.

[17] T. P. Korakianitis, Design of airfoils and cascades of airfoils, *AIAA Journal*, 27 (4) (1989) 455-461.

[18] T. P. Korakianitis, Hierarchical development of three direct-design methods for two-dimensional axial-turbomachinery cascades, *Journal of Turbomachinery*, 115 (2) (1993) 314-324.

[19] T. P. Korakianitis, Prescribed-curvature-distribution airfoils for the preliminary geometric design of axial-turbomachinery cascades, *Journal of Turbomachinery*, 115 (2) (1993) 325-333.

[20] T. P. Korakianitis and P. Papagiannidis, Surface-curvature-distribution effects on turbine-cascade performance, *Journal of Turbomachinery*, 115 (2) (1993) 334-341.

[21] R. Corral and G. Pastor, Parametric design of turbomachinery airfoils using highly differentiable splines, *Journal of Propulsion and Power*, 20 (2) (2004) 335-343.

[22] P. Yi, Y. Wang, X. Sun, D. Huang and Z. Zheng, The effect of variations in first- and second-order derivatives on airfoil aerodynamic performance, *Engineering Applications of Computational Fluid Mechanics*, 11 (1) (2017) 54-68.

[23] I. A. Hamakhan and T. P. Korakianitis, Aerodynamic performance effects of leading-edge geometry in gas-turbine blades, *Applied Energy*, 87 (5) (2010) 1591-1601.

[24] M. G. Turner, A. Merchant and D. Bruna, A turbomachinery design tool for teaching design concepts for axial-flow fans, compressors, and turbines, *Journal of Turbomachinery*, 133 (3) (2011) 031017-1-12.

[25] D. Bruna, C. Cravero, M. G. Turner and A. Merchant, An educational software suite for teaching design strategies for multistage axial flow compressors, *Journal of Turbomachinery*, 134 (5) (2012) 051010-1-8.

[26] K. Siddappaji, M. G. Turner and A. Merchant, General capability of parametric 3D blade design tool for turbomachinery, *ASME Turbo Expo 2012: Turbine Technical Conference and Exposition*, Copenhagen, Denmark (2012) 2331-2344.

[27] A. F. Nemnem, M. G. Turner, K. Siddappaji and M. Galbraith, A smooth curvature-defined meanline section option for a general turbomachinery geometry generator, *ASME Turbo Expo 2014: Turbine Technical Conference and Exposition*, Düsseldorf, Germany (2014) V02BT3 9A026-1-20.

[28] S. M. H. Mahmood, M. G. Turner and K. Siddappaji, Flow characteristics of an optimized axial compressor rotor using smooth design parameters, *ASME Turbo Expo 2016: Turbomachinery Technical Conference and Exposition*, Seoul, South Korea (2016) V02CT45A018-1-12.

[29] K. Balasubramanian, M. G. Turner and K. Siddappaji, Novel curvature-based airfoil parameterization for wind turbine application and optimization, *ASME Turbo Expo 2017: Turbomachinery Technical Conference and Exposition*, Charlotte, North Carolina, USA (2017) V009T49 A020-1-14.

[30] W. Zhang, Z. Zou and J. Ye, Leading-edge redesign of a turbomachinery blade and its effect on aerodynamic performance, *Applied Energy*, 93 (5) (2012) 655-667.

[31] Y. Song and C. Gu, Continuous curvature leading edge of compressor blading, *Journal of Propulsion Technology*, 34 (11) (2013) 1474-1481 (in Chinese).

[32] H. Chen, M. G. Turner, K. Siddappaji and S. M. H. Mahmood, Vorticity dynamics based flow diagnosis for a 1.5-stage high pressure compressor with an optimized transonic rotor, *ASME Turbo Expo 2016: Turbomachinery Technical Conference and Exposition*, Seoul, South Korea (2016) V02AT37A018-1-12.

[33] L. Li, L. Z. Li, L. Ao, Q. Zhou and Z. Yue, 14 Parameters cascade design method with curvature optimization, *Journal of Propulsion Technology*, 34 (1) (2013) 37-41 (in Chinese).

[34] Dakota, *https://dakota.sandia.gov/*.

[35] 3DBGB, *gtsl.ase.uc.edu/3DBGB*.

[36] NUMECA International, *User Manual (Version 8.7)*, NUMECA International, Brussels, Belgium (2010).

[37] J. D. Denton, Lessons from Rotor 37, *Journal of Thermal Science*, 6 (1) (1997) 1-13.

[38] D. Peter and H. W. Donald, Numerical transonic flow field predictions for NASA compressor rotor 37, *ASME 1995 International Gas Turbine and Aeroengine Congress and Exposition*, Houston, Texas, USA (1995) V001T01 A090-1-12.

[39] R. Wang, J. Hu, C. Yu and K. Li, Research on secondary flow vortex structure in transonic compressor rotor, *Journal of Propulsion Technology*, 36 (4) (2015) 504-512.

[40] D. Bruna and M. G. Turner, Isothermal boundary condition at casing applied to the rotor 37 transonic axial flow compressor, *Journal of Turbomachinery*, 135 (3) (2013) 034501-1-4.

[41] M. Drela and M. B. Giles, Viscous-inviscid analysis of transonic and low reynolds number airfoils, *AIAA Journal*, 25 (10) (1987) 1347-1355.

[42] H. H. Youngren and M. Drela, Viscous/inviscid method for preliminary design of transonic cascades, *AIAA/SAE/ASME/ASEE 27th Joint Propulsion Conference*, Sacramento, CA, USA (1991).

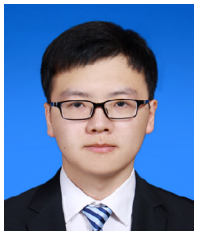

Jieling Li is a master student majoring in Energy and Power Engineering in Harbin Institute of Technology, China. His research direction is aerodynamic design and optimization of high-loaded transonic fans/compressors.

Huanlong Chen, the corresponding author, is a lecturer in HIT, where he received his Ph.D. in School of Energy Science and Engineering in 2009. His research interests include the aerodynamic design and optimization of turbomachinery, the flow diagnoses in turbomachinery with vortex dynamics method, and computational fluid dynamics.